

On the Excess Dispersion in the Polarization Position Angle of Pulsar Radio Emission

Mark M. McKinnon

National Radio Astronomy Observatory, Socorro, NM 87801 USA

ABSTRACT

The polarization position angles (PA) of pulsar radio emission occupy a distribution that can be much wider than what is expected from the average linear polarization and the off-pulse instrumental noise. Contrary to our limited understanding of the emission mechanism, the excess dispersion in PA implies that pulsar PAs vary in a random fashion. An eigenvalue analysis of the measured Stokes parameters is developed to determine the origin of the excess PA dispersion. The analysis is applied to sensitive, well-calibrated, polarization observations of PSR B1929+10 and PSR B2020+28. The analysis clarifies the origin of polarization fluctuations in the emission and reveals that the excess PA dispersion is caused by the isotropic inflation of the data point cluster formed from the measured Stokes parameters. The inflation of the cluster is not consistent with random fluctuations in PA, as might be expected from random changes in the orientation of the magnetic field lines in the emission region or from stochastic Faraday rotation in either the pulsar magnetosphere or the interstellar medium. The inflation of the cluster, and thus the excess PA dispersion, is attributed to randomly polarized radiation in the received pulsar signal. The analysis also indicates that orthogonal polarization modes (OPM) occur where the radio emission is heavily modulated. In fact, OPM may only occur where the modulation index exceeds some critical value, $\beta_c \simeq 0.3$.

Subject headings: Methods: data analysis – polarization – pulsars: general – pulsars: individual (PSR B1929+10, PSR B2020+28)

1. INTRODUCTION

The linear polarization of pulsar radio emission is generally attributed to charged particles streaming along dipolar magnetic field lines above the pulsar's polar cap (Radhakrishnan

¹The National Radio Astronomy Observatory is a facility of the National Science Foundation operated under cooperative agreement by Associated Universities, Inc.

& Cooke 1969). Given the pulsar’s enormous magnetic field strength ($\approx 10^{12}$ gauss) and the stability of its magnetic field structure, as implied by the long term stability of pulsar average profiles (Helfand, Manchester, & Taylor 1975), one might expect the polarization position angle (PA) at a particular pulse longitude to be fixed rigidly on the plane of the sky. However, PA histograms constructed from single-pulse polarization observations are much broader than what is expected from the average linear polarization and the off-pulse instrumental noise (Manchester, Taylor, & Huguenin 1975, hereafter MTH; Stinebring et al. 1984, hereafter SCRWB; McKinnon & Stinebring 1998, hereafter MS1; Karastergiou et al. 2002), suggesting that pulsar PAs also vary in a random fashion.

This excess dispersion in PA may be intrinsic to the pulsar, possibly arising from an analog of stochastic Faraday rotation in the pulsar magnetosphere or from randomly polarized radiation (RPR) in the emission. Since the orientation of a pulsar’s linear polarization vector is thought to be aligned with the magnetic field lines in the emission region, the excess PA dispersion could be due to fluctuations in field line orientation. However, this explanation seems highly unlikely because it requires the orientation of a 10^{12} gauss magnetic field to fluctuate on a timescale comparable with a pulsar’s rotation period ($P \simeq 1$ s). Stochastic Faraday rotation in the interstellar medium (ISM) also seems an unlikely explanation for the origin of the excess PA dispersion because the rotation measure (RM) of the ISM does not fluctuate on the timescale of a rotation period. Furthermore, RM fluctuations should cause PA variations to be similar everywhere within a pulsar’s pulse, but the PA dispersion appears to vary with pulse longitude. Whatever the cause of the excess dispersion, determining it requires a detailed understanding of what causes polarization fluctuations. To discriminate between mechanisms that create polarization fluctuations, analytical tools must be developed for a thorough interpretation of single-pulse polarization observations.

The statistical model of radio polarimetry developed by McKinnon (2003b) provides a foundation for the detailed interpretation of polarization observations. The model accounts for the orthogonally polarized modes (OPM) in the emission and has been used to argue that OPM occur simultaneously, not separately (MS1; McKinnon & Stinebring 2000, hereafter MS2; McKinnon 2002). The model also accounts for deviations from mode orthogonality and has been used to show that the modal connecting bridge in PSR B2016+28 at 1404 MHz is a transition between modes of nonorthogonal polarization (McKinnon 2003a), thereby resolving a possible discrepancy in the interpretation of the pulsar’s viewing geometry (SCRWB). Additionally, the model has been used to show that the large fluctuations in fractional circular polarization observed in pulsar radio emission (SCRWB) may be attributed to the heavy modulation of the mode intensities and the small degree of circular polarization intrinsic to the modes (McKinnon 2002).

The objective of this paper is to derive and apply the analytical tools necessary to determine the origin of the excess PA dispersion in pulsar radio emission. An eigenvalue analysis of radio polarization measurements that is based upon the three-dimensional statistics of radio polarimetry (McKinnon 2003b) is presented in § 2. In the analysis, eigenvalues of polarization measurements are derived for different polarization models, such as fixed polarization, RPR, random fluctuations in PA, OPM, and nonorthogonal polarization modes. The eigenvalue analysis is applied to sensitive, well-calibrated polarization observations of the nearby pulsars PSR B1929+10 and PSR B2020+28 in § 3. The analysis indicates that the excess PA dispersion is caused by RPR in the received pulsar signal. In § 4, the nature of polarization fluctuations in pulsar radio emission is clarified, the origin and consequences of RPR are discussed, and additional applications of the eigenvalue analysis are proposed. The conclusions of the analysis are summarized in § 5.

2. Eigenvalue Analysis of Radio Polarimetry

The Stokes parameters Q , U , and V completely describe the polarization of electromagnetic radiation. Fortunately for radio astronomers, all three Stokes parameters of a radio signal can be measured simultaneously, so the polarization state of the radiation can be completely determined with a single measurement (Radhakrishnan 1999; McKinnon 2003b). When multiple measurements of the Stokes parameters are plotted in a three-dimensional Cartesian coordinate system, or Poincaré space in what follows, the shape of the resulting data point cluster generally resembles an ellipsoid. The location of the ellipsoid’s centroid is given by the average values of the Stokes parameters. The dimensions and orientation of the ellipsoid are determined by polarization fluctuations intrinsic to the radio source and by the instrumental noise. It follows that one may determine what causes the polarization fluctuations provided the dimensions and orientation of the ellipsoid can be measured.

The dimensions and orientation of the polarization ellipsoid can be measured with an eigenvalue analysis of the Stokes parameters. The covariances of the three Stokes parameters form a 3x3 data matrix. The eigenvalues of this covariance matrix are measures of the ellipsoid’s three dimensions. The eigenvectors associated with the eigenvalues are the three axes, or the orientation, of the ellipsoid. The dimensions of the ellipsoid are largely unaffected by whether the source polarization occurs in Q , U , V , or any combination of the three Stokes parameters. Therefore, the eigenvalue analysis and the conclusions drawn from it are generally independent of whether the radio source is linearly-, circularly-, or elliptically-polarized. In the following examples, eigenvalues are derived for different types of mechanisms that create polarization fluctuations.

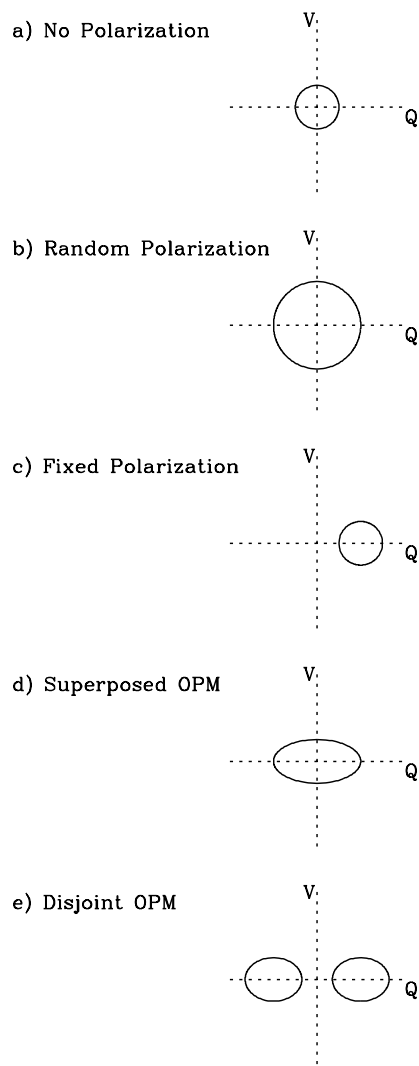


Fig. 1.— Shapes of Q-U-V data point clusters for different types of polarization. The shapes are shown as cross-sections of the cluster in the Q-V plane of Poincaré space. The cluster is a sphere for no polarization (a), random polarization (b), and fixed polarization (c). The cluster resembles a prolate ellipsoid for superposed OPM (d). For disjoint OPM (e), the polarization data reside in two, diametrically-opposed ellipsoids. The signal in (c) and the OPM in (d) and (e) are linearly polarized.

2.1. Fixed Polarization

Let us consider a radio source with constant linear polarization, μ , and assume that its polarization occurs in the Stokes parameter Q. When a radio telescope is pointed towards the source, the measured Stokes parameters are

$$Q = \mu + X_{N,Q}, \quad (1)$$

$$U = X_{N,U}, \quad (2)$$

$$V = X_{N,V}, \quad (3)$$

where X_N is a Gaussian random variable with zero mean and standard deviation, σ_N , that represents the instrumental noise. When multiple measurements of these Stokes parameters are plotted in Poincaré space, the resulting cluster of data points is spherical in shape. The sphere has a radius that is characterized by the magnitude of the instrumental noise, σ_N , and its centroid is offset from the coordinate system origin by a distance μ (Fig. 1c).

The dimensions of the sphere can be determined through an eigenvalue analysis of the Stokes parameters. The matrix formed by the covariances of the Stokes parameters is

$$\bar{C} = \begin{pmatrix} \text{Cov}(Q, Q) & \text{Cov}(Q, U) & \text{Cov}(Q, V) \\ \text{Cov}(U, Q) & \text{Cov}(U, U) & \text{Cov}(U, V) \\ \text{Cov}(V, Q) & \text{Cov}(V, U) & \text{Cov}(V, V) \end{pmatrix} = \sigma_N^2 \begin{pmatrix} 1 & 0 & 0 \\ 0 & 1 & 0 \\ 0 & 0 & 1 \end{pmatrix}. \quad (4)$$

Regardless of radio source polarization, the elements of the covariance matrix are always real and the matrix is always symmetric about its diagonal because the Stokes parameters are always real numbers (i.e., the covariance matrix is always Hermetian). In this particular example, the off-diagonal elements of \bar{C} are equal to zero because the instrumental noise is independent between Stokes parameters (MS1; MS2). Since \bar{C} is symmetric about its diagonal and its off-diagonal elements are equal to zero, the matrix forms the eigenbasis of the data point cluster, and the elements on the matrix diagonal are its eigenvalues. The square root of each eigenvalue is equal to the magnitude of the instrumental noise, σ_N , which is proportional to the size of the sphere's radius. The actual radius of the sphere is about $3\sigma_N$ because the fluctuations in instrumental noise are Gaussian and, thus, approximately 99.73% of the Q-U-V data points reside within a sphere of this radius. Since the eigenvalues are equal to one another, the matrix is triply-degenerate, which means that the eigenvectors corresponding to the eigenvalues do not uniquely define the three axes of the data point cluster, as one would expect for a sphere.

The matrix formed by the second moments of the Stokes parameters is

$$\bar{S} = \sigma_N^2 \begin{pmatrix} 1 + s^2 & 0 & 0 \\ 0 & 1 & 0 \\ 0 & 0 & 1 \end{pmatrix} \quad (5)$$

where $s = \mu/\sigma_N$ is the signal-to-noise ratio in the polarization vector amplitude. The matrix \bar{S} is also an eigenbasis. The principal eigenvector of \bar{S} has an eigenvalue of $\sigma_N^2(1 + s^2)$. It is aligned with the polarization vector of the radio source, which in this example is the Stokes parameter Q.

If the radio source emits RPR, the Q-U-V data point cluster retains its spherical shape, but is inflated by an amount equal to the random polarization fluctuations, σ_P (Fig. 1b). The eigenvalues of the covariance matrix become $\tau_{11} = \tau_{22} = \tau_{33} = \sigma_N^2 + \sigma_P^2$, and the sphere's radius is proportional to the square root of these eigenvalues. If the random polarization fluctuations are also Gaussian, the measured standard deviation in PA is

$$\sigma_\psi = \frac{1}{2\mu}(\sigma_P^2 + \sigma_N^2)^{1/2}. \quad (6)$$

2.2. Random Fluctuations in Position Angle

Stochastic Faraday rotation and random fluctuations in the orientation of a pulsar's magnetic field are possible explanations for the excess PA dispersion in the emission. Both processes can be modeled as random fluctuations in PA. For a linear polarization vector with fixed amplitude and an orientation that randomly varies in the Q-U plane of Poincaré space (i.e. in azimuth only), the measured Stokes parameters are

$$Q = \mu \cos \phi + X_{N,Q}, \quad (7)$$

$$U = \mu \sin \phi + X_{N,U}, \quad (8)$$

$$V = X_{N,V}, \quad (9)$$

where ϕ is a random variable that accounts for the vector's fluctuations in azimuth. If the fluctuations in vector azimuth are Gaussian with zero mean and a standard deviation of σ_ϕ , the measured polarization occurs primarily in Stokes Q, and the eigenvalues of the covariance matrix are

$$\tau_{11} = \frac{\mu^2}{2}[1 - \exp(-\sigma_\phi^2)]^2 + \sigma_N^2, \quad (10)$$

$$\tau_{22} = \frac{\mu^2}{2}[1 - \exp(-2\sigma_\phi^2)] + \sigma_N^2, \quad (11)$$

$$\tau_{33} = \sigma_N^2. \quad (12)$$

The shape of the Q-U-V data point cluster formed by Gaussian fluctuations in PA is a banana-shaped, arcing ellipsoid. The centroid of the arcing ellipsoid resides in the Q-U plane at a distance μ from the origin of Poincaré space. When the PA fluctuations are small ($\sigma_\phi \ll 1$), $\tau_{11} \simeq \tau_{33}$, and the cluster is a prolate ellipsoid (i.e., an ellipsoid that is rotationally symmetric about its major axis). The ellipsoid’s major axis is aligned with the Stokes parameter U because the polarization fluctuations are largest in U (i.e., $\tau_{22} > \tau_{11} > \tau_{33}$). Therefore, the major axis of the ellipsoid is perpendicular to the orientation of the radiation’s polarization vector. Since polarization position angle is related to polarization vector azimuth by $\psi = \phi/2$, the standard deviation in the measured PA is

$$\sigma_\psi = \frac{1}{2}(s^{-2} + \sigma_\phi^2)^{1/2}. \quad (13)$$

2.3. Orthogonal Modes of Polarization

In the statistical model of pulsar polarization proposed by McKinnon & Stinebring (MS1; MS2), the observed polarization is determined by the simultaneous interaction of two, orthogonally polarized modes with randomly varying polarization amplitudes. Since the modes are orthogonal, their polarization vectors lie on the same diagonal in Poincaré space, regardless of the degree of their linear or circular polarization. The statistical model designates the amplitudes of the mode polarizations by the random variables X_1 and X_2 , which have means μ_1 and μ_2 and standard deviations σ_1 and σ_2 , respectively. Assuming for this particular example that the modes are linearly polarized and that their polarization vectors lie along the diagonal aligned with the Stokes parameter Q, the measured Stokes parameters are

$$Q = X_1 - X_2 + X_{N,Q}, \quad (14)$$

$$U = X_{N,U}, \quad (15)$$

$$V = X_{N,V}. \quad (16)$$

If X_1 and X_2 are independent random variables, the covariance matrix computed from these Stokes parameters is

$$\bar{C} = \sigma_N^2 \begin{pmatrix} 1 + \rho^2 & 0 & 0 \\ 0 & 1 & 0 \\ 0 & 0 & 1 \end{pmatrix}, \quad (17)$$

where $\rho = (\sigma_1^2 + \sigma_2^2)^{1/2}/\sigma_N$ is the magnitude of the intrinsic polarization fluctuations relative to the instrumental noise. The shape of the Q-U-V data point cluster formed by superposed

OPM resembles a prolate ellipsoid¹ (see Fig. 1d). The centroid of the ellipsoid is offset from the origin of Poincaré space by a distance $\mu = |\mu_1 - \mu_2|$. The dimensions of the ellipsoid are proportional to the square root of the eigenvalues. The size of the ellipsoid’s major axis scales as $a_1 = \sqrt{\tau_{11}} = \sigma_N(1 + \rho^2)^{1/2}$. The dimensions of the ellipsoid’s minor axes are scaled by the instrumental noise, $a_2 = a_3 = \sigma_N$. The orientations of the ellipsoid’s minor axes are not uniquely determined because the two minor eigenvalues are equal to each other. Unlike the case of random PA fluctuations considered above, the major axis of the OPM ellipsoid is parallel to the radiation’s polarization vector. Thus, the OPM model predicts that the principal eigenvectors determined from the covariances and second moments of the Stokes parameters will be aligned.

The axial ratio of the ellipsoid can be related to the modulation index of the emission. For example, if the modes are completely polarized, the polarization fluctuations are given by $\rho = \beta s$, where β and s are the modulation index and signal to noise ratio, respectively, of the total intensity (McKinnon 2002). The ellipsoid axial ratio is

$$a_1/a_3 = (1 + \rho^2)^{1/2} = (1 + \beta^2 s^2)^{1/2}, \quad (18)$$

which becomes larger as the emission becomes more heavily modulated and as the signal to noise ratio of the observation improves. At the other extreme when the signal to noise ratio is poor or the polarization does not fluctuate (i.e. $\rho = \beta = 0$), the axial ratio approaches unity, and the cluster is a spheroid.

The detailed shape and dimensions of an OPM Q-U-V cluster can be affected by the character of the fluctuations in X_1 and X_2 . Simple numerical simulations of equations 14 through 16 indicate that the cluster resembles a prolate ellipsoid whenever $\sigma_1 \simeq \sigma_2$, regardless of the character of the fluctuations. The simulations also show that Gaussian fluctuations in X_1 and X_2 produce a Q-U-V cluster that is a prolate ellipsoid, even if σ_1 differs from σ_2 . When X_1 and X_2 are exponential random variables with $\sigma_1 \gg \sigma_2$, the ellipsoid is still rotationally symmetric about its major axis, but the ellipsoid is stretched along its major axis in the direction of the dominant mode, X_1 . This is to be expected because the polarization fluctuations would be largely determined by the dominant mode. The dimensions of the cluster’s minor axes extend about $\pm 3a_2$ and $\pm 3a_3$ from the cluster centroid because the size of the minor axes are set by the Gaussian instrumental noise. The size of the cluster’s major axis extends about $\pm 3a_1$ from the centroid if the mode polarizations are Gaussian random variables and can be larger if they are exponential random variables.

¹Even if the mode polarization amplitudes are not independent, the cluster is still a prolate ellipsoid but with a principal eigenvalue of $\tau_{11} = \sigma_1^2 + \sigma_2^2 - 2r_{12}\sigma_1\sigma_2 + \sigma_N^2$, where r_{12} is the correlation coefficient of the polarization amplitudes (MS1).

If OPM are disjoint (i.e. occur separately) instead of superposed, the Q-U-V data points will reside in two ellipsoids that are diametrically opposed in Poincaré space (Fig. 1e). The size of the ellipsoids’ minor axes are set by the instrumental noise. The size of the ellipsoids’ major axes are determined by the instrumental noise and the polarization fluctuations of the modes.

2.4. Nonorthogonal Polarization Modes

Nonorthogonal polarization modes do not occur along the same diagonal in Poincaré space. However, the two vectors representing the modes still define a plane, and the orientation of this plane depends upon the elliptical polarization of the modes. Here, and without loss of generality, the modes are assumed to be linearly polarized. If the deviation from orthogonality is given by the angle θ , incorporating the nonorthogonality of the modes in the model described above (McKinnon 2003a) gives the following expressions for the measured Stokes parameters.

$$Q = X_1 - X_2 \cos \theta + X_{N,Q}, \quad (19)$$

$$U = X_2 \sin \theta + X_{N,U}, \quad (20)$$

$$V = X_{N,V}. \quad (21)$$

If the mode polarizations are independent (i.e., $\text{Cov}(X_1, X_2) = 0$), the covariance matrix for the nonorthogonal modes is

$$\bar{C} = \begin{pmatrix} \sigma_1^2 + \sigma_2^2 \cos^2 \theta + \sigma_N^2 & -\sigma_2^2 \cos \theta \sin \theta & 0 \\ -\sigma_2^2 \cos \theta \sin \theta & \sigma_2^2 \sin^2 \theta + \sigma_N^2 & 0 \\ 0 & 0 & \sigma_N^2 \end{pmatrix}. \quad (22)$$

The eigenvalues of the covariance matrix in equation 22 are

$$\tau_{11} = \frac{1}{2} \left[(\sigma_1^2 + \sigma_2^2 + 2\sigma_N^2) + \sqrt{\sigma_1^4 + \sigma_2^4 + 2\sigma_1^2\sigma_2^2 \cos(2\theta)} \right], \quad (23)$$

$$\tau_{22} = \frac{1}{2} \left[(\sigma_1^2 + \sigma_2^2 + 2\sigma_N^2) - \sqrt{\sigma_1^4 + \sigma_2^4 + 2\sigma_1^2\sigma_2^2 \cos(2\theta)} \right], \quad (24)$$

$$\tau_{33} = \sigma_N^2. \quad (25)$$

The shape of the Q-U-V data point cluster formed by nonorthogonal polarization modes also resembles an arcing ellipsoid because the nonorthogonal mode breaks the symmetry of the cluster.

3. APPLICATION OF EIGENVALUE ANALYSIS

The eigenvalue analysis developed in § 2 was applied to sensitive, well-calibrated, polarization observations of PSR B2020+28 and PSR B1929+10 to determine the origin of the excess PA dispersion. The observations were made by SCRWB with the Arecibo radio telescope at a frequency of 1404 MHz. At the time the observations were made, the telescope’s nominal system temperature was 40 K, and its forward gain was 8 K/Jy. Data from the same observations were used in the analyses documented in MS1, MS2, and McKinnon (2003a). SCRWB’s superb polarization calibration is essential to the success of the eigenvalue analysis because improper or inadequate calibration will alter the dimensions of the Q-U-V data point cluster, and thus adversely influence the conclusions drawn from the analysis. To insure that the observed polarization fluctuations were intrinsic to the pulsar, and not due to slowly-varying signal amplification caused by diffractive interstellar scintillation (MS1), a subset of the overall time series where the running mean intensity did not vary was selected for further analysis. The time series thus selected contained 800 pulses for PSR B2020+28 and 4000 pulses for PSR B1929+10. The pulse profiles and modulation indices computed from the selected time series are shown in Figure 2.

The eigenvalue analysis was performed as follows. For both pulsars, a covariance matrix of the Stokes parameters Q, U, and V was computed at each pulse phase bin. The covariances were then used to calculate the eigenvalues and eigenvectors of the matrix. As illustrated by the examples in § 2, the dimensions of the Q-U-V ellipsoid at each phase bin were estimated by taking the square root of the eigenvalues. Examples of Q-U-V ellipsoids for each pulsar are shown in Figures 3 and 5. In each panel of both figures, every data point has been rotated by the PA at the relevant phase bin so that the major axis of the polarization ellipsoid occurs in the Q-V plane of Poincaré space. The rotation eliminates projection effects in the data presentation. The bottom panels of Figure 6 show how the ellipsoid axial ratios vary across the pulse of each pulsar. The ratio of the ellipsoid’s largest dimension to its smallest dimension, a_1/a_3 , is shown by the solid line in the bottom panels of the figure. The ratio of the ellipsoid’s two smaller dimensions, a_2/a_3 , is shown by the dotted line in the same panels.

Eigenvalues and eigenvectors were also computed from the second moments of the Stokes parameters to insure that this new data analysis method reproduced the results obtained from more traditional methods. As predicted by the eigenvalue analysis, the PAs of polarization vectors given by the second moment principal eigenvectors were very similar to the PAs computed in the traditional way,

$$\psi = \frac{1}{2} \arctan\left(\frac{U}{Q}\right). \quad (26)$$

Furthermore, the vector colatitude given by the second moment principal eigenvector was

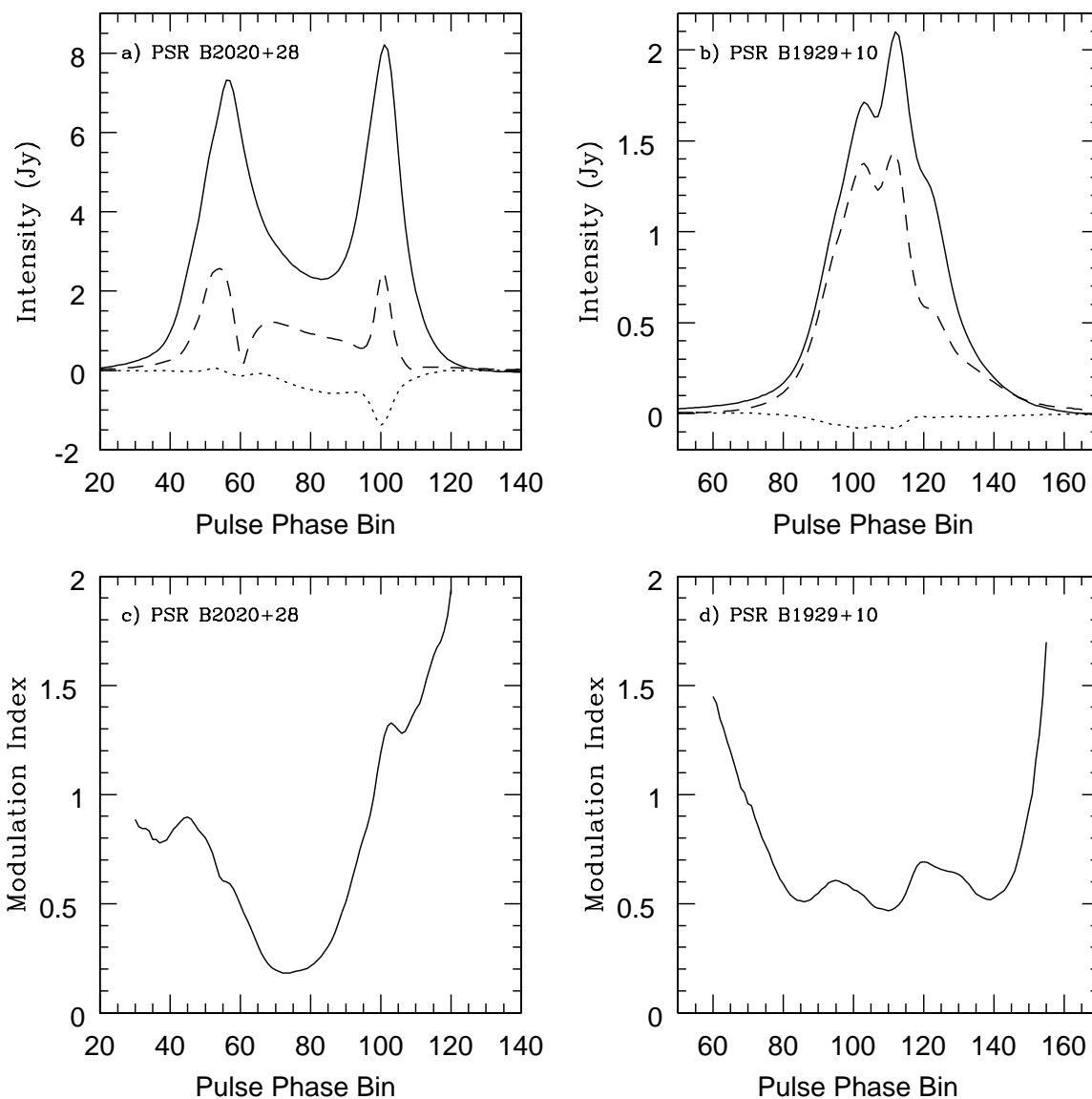


Fig. 2.— Pulse profile and intensity modulation indices of PSR B2020+28 and PSR B1929+10 at 1404 MHz. The average profiles of the two pulsars are shown in the top panels. Total intensity, linear polarization, and circular polarization are denoted by the solid, dashed, and dotted lines, respectively. The bottom panels show how the total intensity modulation index varies across the pulse of each pulsar.

very similar to the colatitude traditionally calculated from

$$\theta = \arccos \left[\frac{V}{(Q^2 + U^2 + V^2)^{1/2}} \right]. \quad (27)$$

3.1. PSR B2020+28

Figure 3 shows four examples of Q-U-V data point clusters in PSR B2020+28 and provides the clue that explains the excess PA dispersion in the pulsar. Data recorded off the pulse are shown by the cluster at phase bin 10. The cluster has the spheroidal shape and size expected for instrumental noise. The cluster’s values of a_1 , a_2 , and a_3 are equal to each other and are equal to the noise calculated off the pulse, $\sigma_N = 0.1$ Jy. These values suggest that the cluster’s three dimensions are equal and, consequently, that the cluster is spheroidal in shape. All the Q-U-V data points at bin 10 reside within a sphere of radius, $r = 3\sigma_N$. But contrary to most examples given in § 2, the smallest dimension of every other cluster shown in Figure 3, as indicated by the values of a_3 , is much greater than what is expected from the instrumental noise.

At phase bin 74, the cluster is a spheroid that is three times larger than what is expected from the off-pulse noise. The fact that the cluster at bin 74 is a spheroid, and not an arcing ellipsoid, suggests that the excess PA dispersion at this pulse location is not caused by random fluctuations in PA (e.g. stochastic Faraday rotation or fluctuations in the orientation of magnetic field lines). Since the data point cluster is not a prolate ellipsoid, the data do not support the assumption of MS1 and MS2 that both polarization modes occur at bin 74 of PSR B2020+28. The large size of the spheroid, as well as the large values of a_3 at bins 61 and 91, suggests that the excess PA dispersion is caused by a mechanism that isotropically inflates the clusters. The only mechanism considered in § 2 that can isotropically inflate the cluster is RPR in the received signal.

Another intriguing and noteworthy feature of the data at bin 74 is that the fluctuations in total intensity and polarization are Gaussian-like (see Fig. 4 and Figs. 4 & 7 of MS1). This is in stark contrast to intensity fluctuations in other pulsars, which can be lognormal, power law, and chi-squared or gamma (e.g., Cairns, Johnston, & Das 2003; Cairns et al. 2003; MS1; Cordes 1976a, 1976b). The emission’s extremely low modulation index near the center of the pulse is also indicative of Gaussian intensity fluctuations. Since total intensity must be non-negative, Gaussian intensity fluctuations require the mean intensity, μ_I , to be at least a factor of three to five times greater than the intensity standard deviation, σ_I . Therefore, the modulation index of Gaussian fluctuations must satisfy $\beta = \sigma_I/\mu_I < 0.2 - 0.3$. Interestingly, at phase bins 65 to 85 where the modulation index is $\beta < 0.3$, the Q-U-V data point clusters

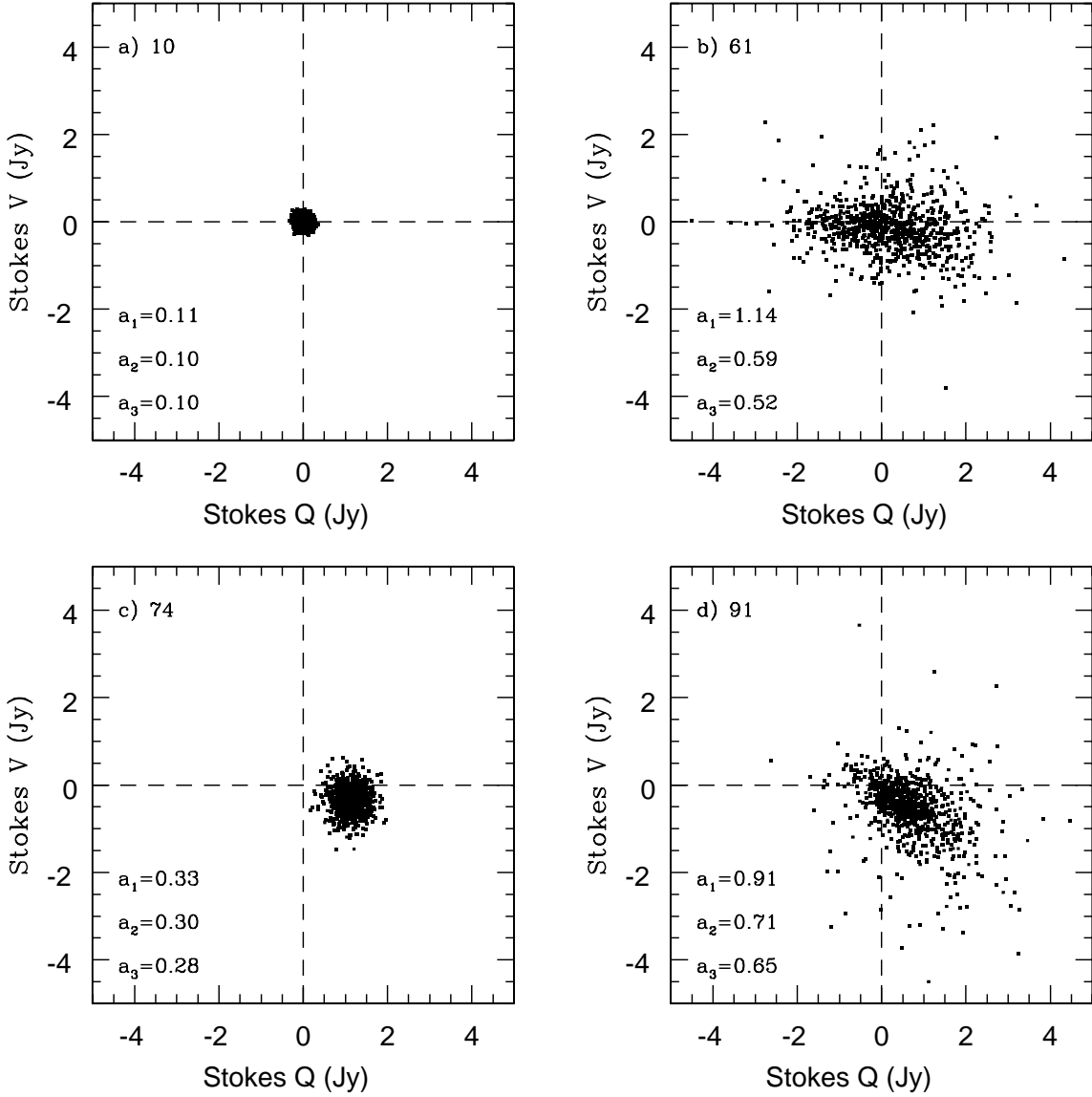


Fig. 3.— Q-U-V data point clusters at different locations in the pulse of PSR B2020+28. The pulse phase bin is denoted in the upper left corner of each panel. The quantities a_1 , a_2 , and a_3 in the bottom left corner of each panel are the square roots of the cluster eigenvalues, in units of Jy, and are proportional to the size of the cluster’s three dimensions. For display purposes, the data points have been rotated so that the major axis of the cluster occurs in the Q-V plane of Poincaré space. OPM occur at bins 61 and 91, but only one polarization mode occurs at bin 74. The overall size of each cluster is much larger than the off-pulse noise at bin 10, suggesting that randomly polarized radiation accompanies the radio emission.

also have spheroidal shapes, similar to that of bin 74. Thus, the polarization properties at bins 65 through 85 are similar to those at bin 74.

The simplest explanation for the Q-U-V data point cluster at bin 74 is a combination of a fixed polarization vector, RPR, and instrumental noise. If this hypothesis is correct, the observed Gaussian fluctuations in polarization would be due to a combination of RPR and instrumental noise because the polarization vector is assumed to have a fixed amplitude. Furthermore, the distributions of PA, linear polarization, and circular polarization should all be broadened by the fluctuations due to RPR. To test this hypothesis, histograms of linear polarization, circular polarization, and PA constructed from the bin 74 polarization data were compared to the theoretical distributions expected for a fixed polarization vector in Gaussian noise (McKinnon 2002), where the noise is due to a combination of RPR and instrumental noise.

$$f_{\psi}(\psi) = \frac{1}{\pi} \exp\left(-\frac{\mu_L^2}{2\sigma^2}\right) \left\{ 1 + \sqrt{\frac{\pi}{2}} \frac{\mu_L}{\sigma} \cos(2\psi) \exp\left(\frac{\mu_L^2}{2\sigma^2} \cos^2(2\psi)\right) \left[1 + \operatorname{erf}\left(\frac{\mu_L \cos(2\psi)}{\sigma \sqrt{2}}\right) \right] \right\} \quad (28)$$

$$f_L(x) = \frac{x}{\sigma^2} \exp\left[-\frac{(\mu_L^2 + x^2)}{2\sigma^2}\right] I_0\left(\frac{x\mu_L}{\sigma^2}\right) \quad (29)$$

$$f_V(x) = \frac{1}{\sigma\sqrt{2\pi}} \exp\left[-\frac{(x - \mu_V)^2}{2\sigma^2}\right] \quad (30)$$

The parameters used to construct the theoretical distributions were obtained from the experimental data. The mean circular polarization was $\mu_V = -0.32$ Jy, the mean linear polarization was $\mu_L = (\mu_Q^2 + \mu_U^2)^{1/2} = 1.11$ Jy, and the standard deviation of the Gaussian noise was taken from the bin 74 data point cluster as $\sigma = 0.30$ Jy. As shown in Figure 4, the theoretical distributions compare extremely well with the measured histograms. The comparison of the PA distributions is much more favorable than the result obtained by MS1² where identical data were used but the standard deviation of the Gaussian noise was assumed to be $\sigma = 0.1$ Jy, instead of 0.3 Jy, in the calculation of the theoretical distribution. In summary, the favorable comparison between the theoretical and measured distributions in Figure 4 confirms a simple interpretation of the emission’s polarization properties at bin 74. The Gaussian fluctuations in polarization are due to RPR and instrumental noise. These fluctuations broaden the PA distribution as well as the distributions of linear and circular polarization. Therefore, the excess dispersion in PA is due solely to RPR. Another component of the emission has a polarization vector with fixed amplitude and orientation. Consequently, only one polarization mode with constant polarization occurs at bin 74.

²The histograms in Figs. 7b and 7d of MS1 utilize smaller bin sizes than those of Fig. 4. Therefore, the histograms appear to be slightly different, although the same data were used in the two figures.

Given this interpretation, one may also say something about the fluctuations in total intensity at bin 74. Since the mode’s polarization is constant, the mode’s intensity must also be constant because it is highly unlikely that the mode’s intensity can randomly fluctuate while its polarization remains constant, particularly when the mode is completely polarized as assumed in MS1 and MS2. Therefore, the observed fluctuations in total intensity at bin 74 cannot be attributed to the polarization mode. They must be due to RPR.

Gaussian fluctuations and random polarization are properties of instrumental noise. However, the inflation of the Q-U-V data point clusters cannot be attributed to on-pulse instrumental noise. At bin 74, the average total intensity is 2.7 Jy, or an antenna temperature of 21.6 K. This change in antenna temperature would increase the noise by no more than a factor of 1.5 (see eqn. (B4) of MS2), far short of the factor of three required to explain the size of the cluster. Furthermore, different locations within the pulse of PSR B2020+28 have similar total intensities, but the smallest dimensions of the clusters at these locations are very different (Fig. 6), suggesting that the mechanism that inflates the cluster is not instrumental in origin. Also, the inflation of the clusters cannot be attributed to the correlation of on-pulse instrumental noise between Stokes parameters. Correlated instrumental noise will stretch a cluster in one dimension, instead of inflating it, because correlated data points will tend to form a straight line in Poincaré space. For example, in the extreme case when the instrumental noise is completely correlated between the Stokes parameters, all elements of the covariance matrix will be σ_N^2 . The matrix eigenvalues will be $\tau_{11} = 3\sigma_N^2, \tau_{22} = \tau_{33} = 0$, which indicate that the data point cluster is one-dimensional.

Superposed OPM definitely occur at bins 61 and 91 of PSR B2020+28 because the data point clusters at these locations are elongated along the line that passes through the cluster centroid and the Q-V origin (the diagonal in Poincaré space). The simple fact that the cluster at each bin resembles a single, prolate ellipsoid and not two distinct ellipsoids suggests that OPM in this pulsar are superposed, not disjoint. At bin 61, the modes are primarily linearly polarized because the ellipsoid’s major axis does not tilt much from $V = 0$. If the polarization data at bin 61 were plotted in a PA histogram, the modes would be shown to occur with nearly equal frequency (see Fig. 5 of MS1) because the ellipsoid centroid roughly coincides with the Q-V origin and the number of data points on either side of $Q = 0$ is about the same. At bin 91, the modes have a significant degree of circular polarization, as indicated by the ellipsoid’s tilt. One mode would occur much more frequently than the other in a PA histogram because most data points have $Q > 0$. RPR also accompanies the modes at these pulse locations because the two smaller ellipsoid dimensions indicated by a_2 and a_3 are approximately equal but are much larger than the instrumental noise.

Figure 6 indicates where OPM occur in the pulse of PSR B2020+28 and shows how the

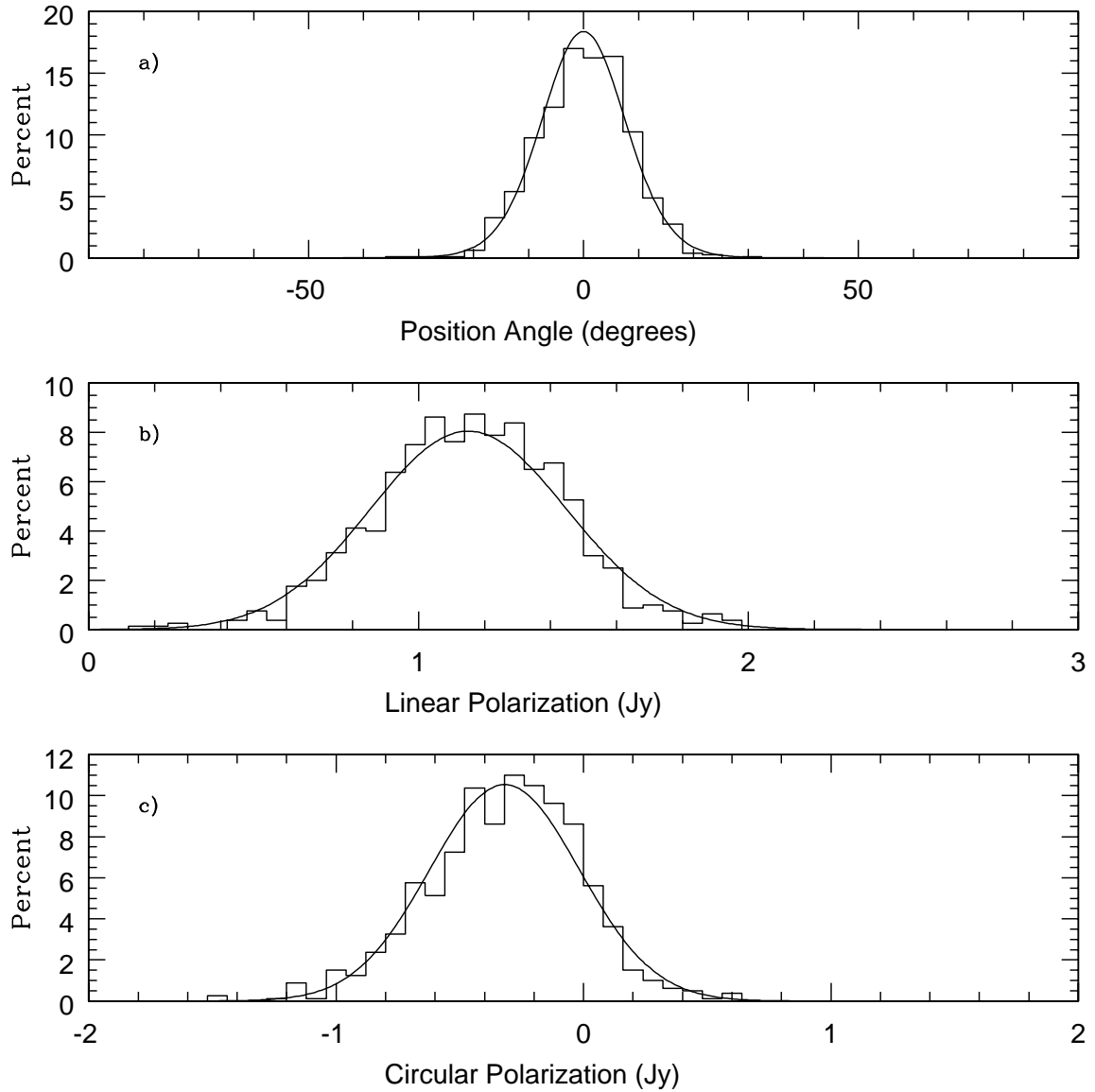


Fig. 4.— Distributions of polarization position angle (a), linear polarization (b), and circular polarization (c) at pulse phase bin 74 of PSR B2020+28. The histograms were constructed from measured polarization values. The solid, continuous lines in each panel are the theoretical distributions expected for a fixed polarization vector and Gaussian noise.

magnitude of RPR may vary across it. The RPR magnitude, as estimated from the value of a_3 for each cluster and the off-pulse instrumental noise,

$$\sigma_P = (a_3^2 - \sigma_N^2)^{1/2}, \quad (31)$$

is shown in Figure 6a. The magnitude of RPR is small in comparison to the total intensity at every location within the pulse. In Figure 6c, the large ratios of the ellipsoids’ major and minor axes, a_1/a_3 , indicate where OPM occur, primarily in the peaks and wings of the pulse. The intensity modulation index is large (Fig. 2c) at the same locations. The ratio of the ellipsoids’ smaller dimensions is $a_2/a_3 \simeq 1$ everywhere in the pulse, indicating that the ellipsoids are generally rotationally symmetric about their major axes as predicted by the OPM statistical model. If the small deviations from axial symmetry are real, they may be due to a slight nonorthogonality in the pulsar’s polarization modes (McKinnon 2003a). The axial ratios and the modulation indices are small near the pulse center where it is possible that only one polarization mode with fixed polarization occurs.

3.2. PSR B1929+10

Figure 5 shows examples of Q-U-V data point clusters in PSR B1929+10. Again, the cluster representing the data recorded off the pulse has the spheroidal shape and size expected for the instrumental noise. The magnitude of the noise is smaller than that for PSR B2020+28 primarily because a larger bandwidth was used for the PSR B1929+10 observation. The smallest dimension of each ellipsoid is about a factor of two larger than expected from the instrumental noise, suggesting that the signal received from the pulsar contains RPR.

The clusters at phase bins 90, 119, and 125 are highly elongated, single ellipsoids, indicating the presence of superposed polarization modes. Since the data at each bin do not reside in two distinct clusters, the observations do not support the hypothesis of disjoint polarization modes. The superposed modes are primarily linearly polarized because the major axis of each ellipsoid is nearly aligned with $V = 0$. Although both polarization modes occur at bin 90, as indicated by its highly elongated Q-U-V cluster, only one mode will appear in a PA histogram computed from these data because the vast majority of data points have $Q > 0$. This simply means that one polarization mode is much stronger than the other (i.e., $\mu_1 \gg \mu_2$). At phase bins 119 and 125, both polarization modes will appear in PA histograms because data points in these Q-U-V clusters reside on either side of $Q = 0$. In both cases, one mode will occur more frequently than the other because more data points have $Q > 0$ than $Q < 0$. Figure 5 of McKinnon (2003a) shows the PA histogram for bin 119. The polarization

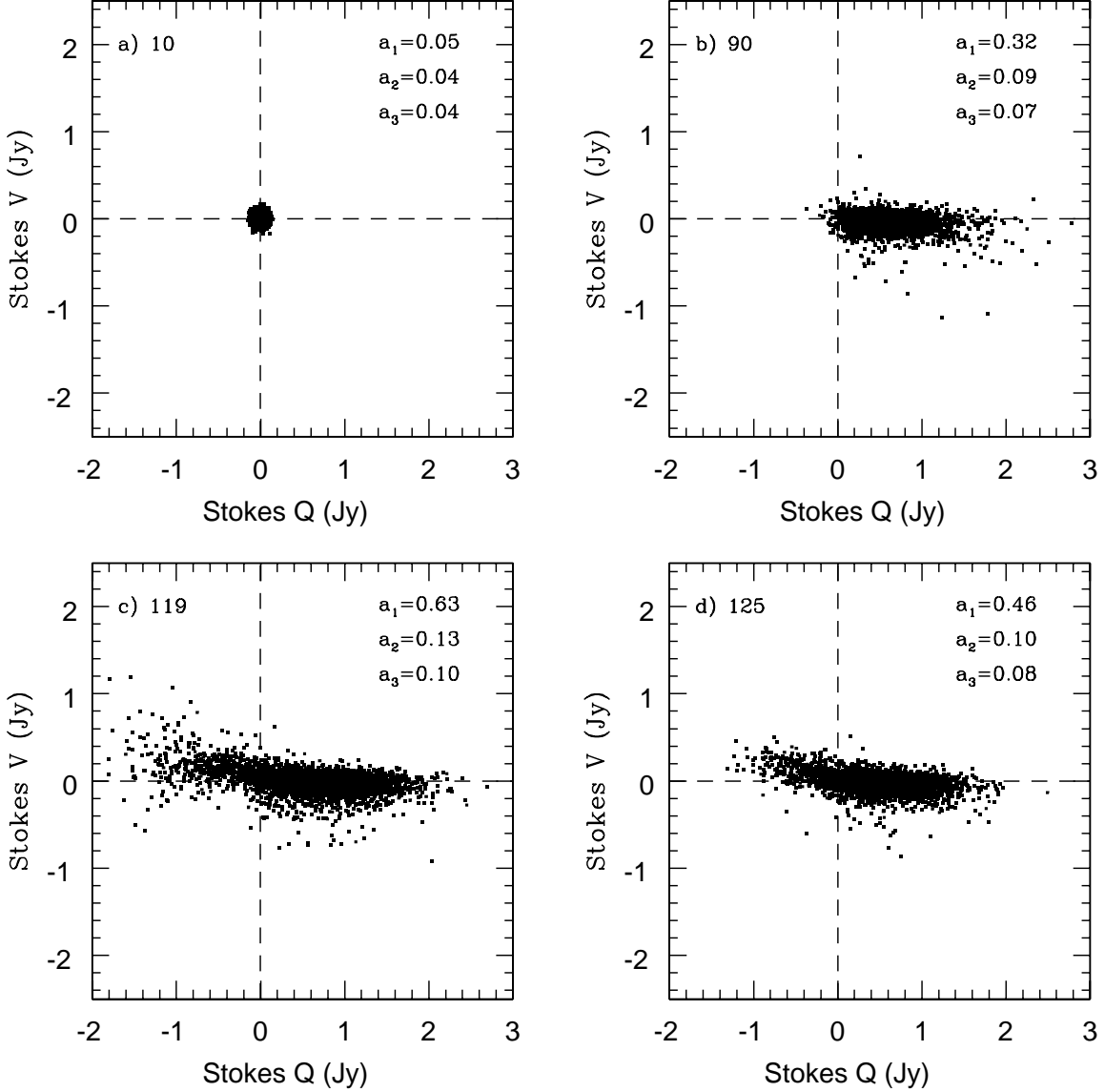


Fig. 5.— Q-U-V data point clusters at different locations in the pulse of PSR B1929+10. The pulse phase bin is denoted in the upper left corner of each panel, and the square roots of the cluster eigenvalues are listed in the upper right corner. The data points have been rotated so that the major axis of the cluster occurs in the Q-V plane of Poincaré space. OPM occur at each bin where the cluster is highly elongated. The modes at bins 119 and 125 are not truly orthogonal because not all data points reside near the same diagonal. Similar to PSR B2020+28, the overall size of each cluster is larger than the off-pulse noise (bin 10).

modes at phase bins 119 and 125 are not precisely orthogonal because not all the data points in the Q-U-V clusters reside near a diagonal in Poincaré space. These clusters are consistent with what is expected for superposed, nonorthogonal polarization modes (see § 2.4 above and McKinnon 2003a). Historically, cases of nonorthogonal polarization modes have been documented with PA histograms (Backer & Rankin 1980; SCRWB; McKinnon 2003a), which give no indication that the nonorthogonality may also occur in circular polarization. When the Q-U-V data are reported as polarization ellipsoids, the nonorthogonality in circular polarization is readily apparent.

Figure 6b shows how the magnitude of RPR, as estimated from equation 31, varies across the pulse of PSR B1929+10. As with PSR B2020+28, the RPR in PSR B1929+10 cannot be attributed to on-pulse instrumental noise because the total intensity of the pulsar cannot increase the noise by the factor required by the smallest dimensions of the polarization ellipsoids. The magnitude of RPR in PSR B1929+10 is much less than that in PSR B2020+28.

The shapes of the polarization ellipsoids in the pulse of PSR B1929+10 are consistent with the statistical model of superposed polarization modes. As shown in Figure 6d, the axial ratios of the ellipsoids are generally consistent with the prolate ellipsoidal shape predicted by the model. Near the center of the pulse, the ratios of the ellipsoids’ minor axes are slightly greater than one, indicating that the ellipsoids are not perfectly symmetric about their major axes. The slight asymmetry is most likely due to the nonorthogonality of the polarization modes. At phase bins 95 through 125, both the ellipsoid axial ratio and the intensity modulation index (Fig. 2d) are relatively constant at $a_1/a_3 \simeq 6.6$ and $\beta \simeq 0.55$, respectively, indicating that both polarization modes occur where the emission is heavily modulated. Throughout the pulse of PSR B1929+10, the modulation index is not consistent with Gaussian fluctuations in total intensity.

SCRWB specifically commented on the very narrow distributions of PA and fractional circular polarization in PSR B1929+10. The PA distribution was the narrowest of the pulsars they studied, and they attributed the high degree of PA stability to an extremely homogeneous emission region. The supplemental information provided to SCRWB’s interpretation by the eigenvalue analysis is any fluctuations in PA and fractional circular polarization in excess of the instrumental noise may be attributed to RPR in the received signal.

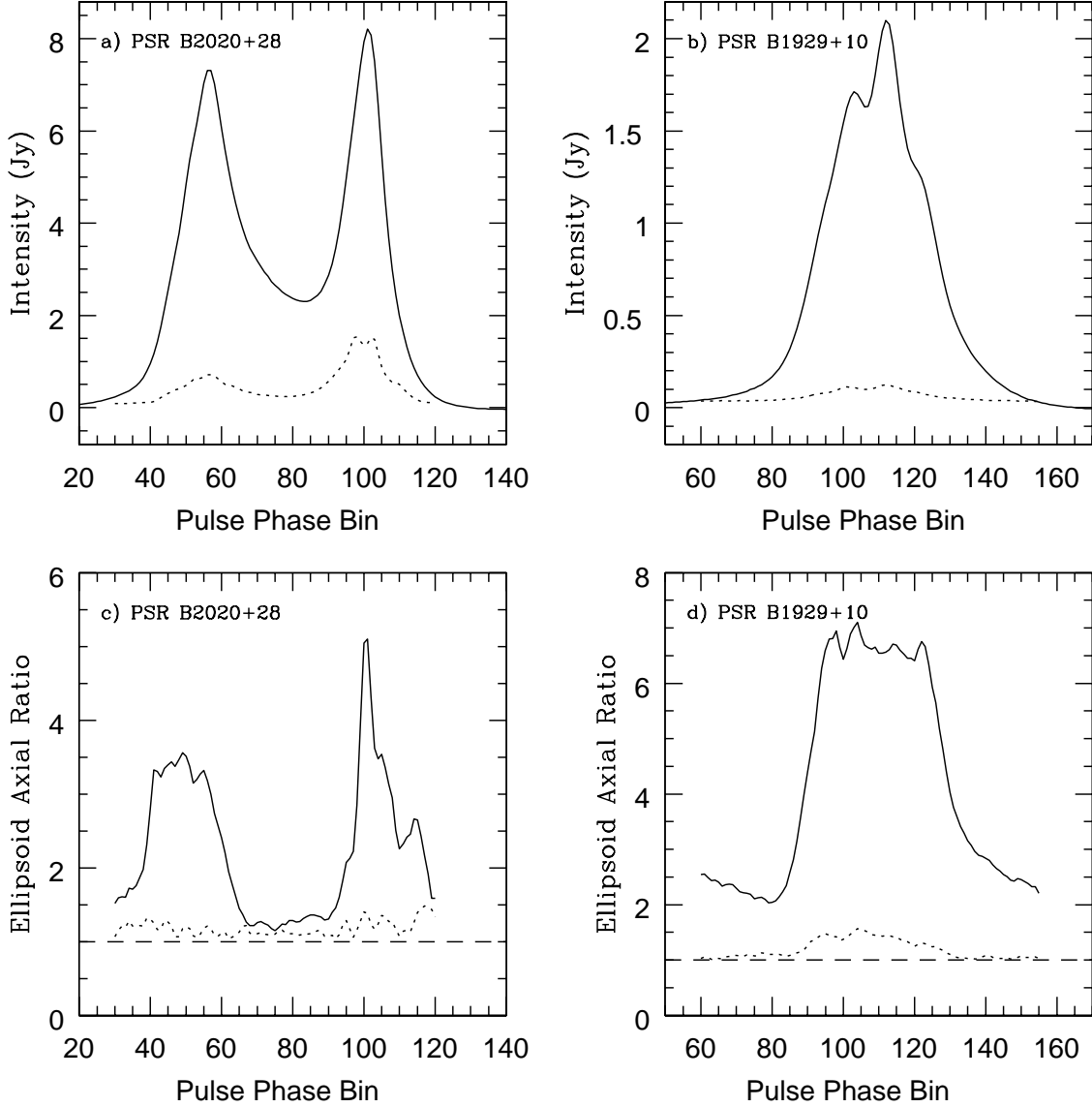


Fig. 6.— Randomly polarized radiation (RPR) and the relative dimensions of the polarization ellipsoids in PSR B2020+28 and PSR B1929+10. The top panels show the total intensity (solid line) and the magnitude of RPR (dotted line) for each pulsar. The bottom panels show the relative dimensions of the polarization ellipsoids for each pulsar. The solid line is the ratio of the largest to the smallest ellipsoid dimension, and the dotted line is the ratio of the two smaller ellipsoid dimensions. The ratios indicate that the ellipsoids are generally prolate, a result that is consistent with the statistical model of superposed OPM.

4. DISCUSSION

Three-dimensional measurements can assume a variety of shapes and sizes, and axial and eigenvalue ratios are often used to characterize these types of measurements (Fisher, Lewis, & Embleton 1987). Obviously, any model that hopes to describe the data must be able to reproduce the fundamental shape of the three-dimensional data set. The shapes and axial ratios of the data point clusters in PSR B2020+28 and PSR B1929+10 are consistent with the predictions of the statistical model of radio polarimetry (McKinnon 2003b). The model predicts that the clusters are prolate ellipsoids when superposed OPM occurs and are spheroids when the polarization is fixed. Clearly, the data are not consistent with some other cluster shape (e.g., dual ellipsoids or an oblate ellipsoid) that might be predicted by some other model (e.g., disjoint OPM).

In summarizing their comprehensive polarization observations, SCRWB favored a modal broadening mechanism as an explanation for the broad PA histograms they observed. However, they also allowed that the histograms could be explained by the superposition of OPM and RPR provided that a technique could be developed to separate the random component from the modal emission. Their interpretation also required the random component to be small in comparison to the modal emission. The analysis presented in this paper is a technique that allows the component separation to be made. In the analysis, RPR appears as the isotropic inflation of the Q-U-V data point cluster, and OPM manifests itself as an elongation of the cluster along a diagonal in Poincaré space. When the eigenvalue analysis is applied to the observational data, the random component is found to be smaller than the modal emission as indicated by the large axial ratios of the clusters (Fig. 6). Expressed mathematically, the superposition of OPM and RPR represents a general statistical model for a polarized signal received from a pulsar.

$$Q = \sin \theta_o \cos \phi_o (X_1 - X_2) + X_{P,Q} + X_{N,Q}, \quad (32)$$

$$U = \sin \theta_o \sin \phi_o (X_1 - X_2) + X_{P,U} + X_{N,U}, \quad (33)$$

$$V = \cos \theta_o (X_1 - X_2) + X_{P,V} + X_{N,V}. \quad (34)$$

Here, θ_o and ϕ_o are the colatitude and azimuth, respectively, of the OPM polarization vectors (McKinnon 2003b), and X_P is a random variable representing RPR. This is not to say that X_1 , X_2 , and X_P always occur at every pulse longitude of every pulsar. It is conceivable that any one, or even all, of these components could be absent from the received signal.

Karastergiou, Johnston, & Kramer (2003) offer a slightly different interpretation of the polarization fluctuations in pulsar radio emission. They suggest that in addition to the OPM fluctuations that occur along a diagonal in Poincaré space, the orientation of the diagonal

randomly varies. Their interpretation does not include RPR. The Karastergiou et al. model can be represented by equations (32)–(34) if the RPR terms, X_P , are ignored and if the angles θ_o and ϕ_o are allowed to be random variables.

The phrases “randomly polarized radiation”, “unpolarized radiation”, and “randomization of position angle” describe very different polarization processes, but they are occasionally used interchangeably in the pulsar literature, particularly in interpretative discussions of mode-separated pulse profiles, single-pulse polarization observations, and radiation depolarization mechanisms. The differences between these processes must be explicitly described to avoid confusion in the use of the phrases. The Stokes parameters Q, U, and V recorded in an observation of an unpolarized radio source are consistent with instrumental noise. In Poincaré space, they occupy a sphere of radius $r = 3\sigma_N$ centered on the origin (Fig. 1a). While RPR is unpolarized on average, it is not the same as unpolarized radiation. The Stokes parameters recorded in an observation of a randomly polarized radio source will also appear as a sphere centered on the origin of Poincaré space (Fig. 1b), but the sphere’s radius will be $r = 3(\sigma_P^2 + \sigma_N^2)^{1/2}$, where σ_P accounts for the random polarization fluctuations intrinsic to the source. The phrase “randomization of position angle” implies fluctuations in the PA of a linear polarization vector which are restricted to the Q-U plane of Poincaré space. Polarization observations of a radio source with random PA fluctuations will appear as an arcing ellipsoid. The two largest dimensions of the ellipsoid will correspond to eigenvectors in the Q-U plane. The ellipsoid’s centroid will be offset from the origin by a distance equal to the polarization of the source.

The Gaussian intensity fluctuations and the random polarization observed at the center of the PSR B2020+28 pulse suggest a possible origin of RPR. Pulsar radio emission has been described as an incoherent addition of individually coherent shot pulses (Rickett 1975; Cordes 1976a, 1976b; Hankins et al. 2003). The addition can occur within the telescope receiving system, in the dispersion and scattering of the pulses as they propagate through the ISM, and at the pulsar if many independent emission events contribute to the instantaneous signal (Cordes 1976a, 1976b). From the Central Limit Theorem, the recorded signal will have Gaussian statistics regardless of the intensity distribution of the shot pulses, provided the number of pulses in the incoherent sum is very large. If the shot pulses also have no preferred polarization, the polarization of the recorded signal will be completely random. This scenario suggests that the intensity and polarization of the RPR component (X_P in eqns. (32)–(34)) always follow Gaussian statistics. It is difficult to extract the statistics of X_P in PSR B1929+10 and at other locations within PSR B2020+28 because of the large polarization fluctuations due to OPM. Cairns et al. (2003) have found evidence for a small Gaussian emission component in the Vela pulsar using theoretical models of its longitude-dependent intensity distributions. They also attribute the Gaussian component to the incoherent sum

of shot pulses.

The eigenvalue analysis may be used to determine how pulsar radio emission depolarizes at high frequency (Manchester, Taylor, & Huguenin 1973; Morris, Graham, & Sieber 1981). The depolarization has been attributed to OPM, randomization of PA, a process intrinsic to the emission mechanism, or any combination of the three (MTH; SCRWB; Xilouris et al. 1994; McKinnon 1997; MS1; Karastergiou et al. 2002). Since the observed Q-U-V clusters are not the arcing ellipsoids expected for fluctuations in PA, the analysis presented here suggests that randomization of PA does not occur. Therefore, randomization of PA is not a strong candidate for a depolarization mechanism. However, the analysis indicates that RPR occurs in the received pulsar signal, and RPR may be a viable depolarization mechanism if it is generated at emission. Applying the eigenvalue analysis to high frequency polarization observations of pulsars may determine if OPM, RPR, or both lead to the depolarization. OPM will be the depolarization mechanism if the high frequency Q-U-V clusters are highly elongated ellipsoids with dimensions of their minor axes set by the instrumental noise. Since the radiation is depolarized, the cluster centroid should be located near the origin of Poincaré space. If RPR depolarizes the emission, the high frequency Q-U-V clusters will be spheroids with radii much larger than the instrumental noise and with centroids near the Poincaré origin. Applying the eigenvalue analysis to multi-frequency, polarization observations of pulsars can also be used to measure the spectrum of RPR and the longitudinal extent of OPM, both of which will be useful in determining the depolarization mechanism.

The presence of RPR in the received signal has other subtle, yet important, consequences for pulsar polarization observations and our interpretation of them. Perhaps the most important consequence of RPR is that it masquerades as on-pulse instrumental noise, thereby causing histograms of linear polarization, circular polarization, polarization position angle, fractional linear polarization, and fractional circular polarization to be much wider than what is expected from the off-pulse instrumental noise. McKinnon (2002) derived the statistics of fractional polarization in an attempt to explain the large dispersion in fractional circular polarization reported by SCRWB. The excess dispersion was attributed to a combination of the signal-to-noise ratio of the observations, the heavy modulation of the mode intensities, and the small degree of circular polarization intrinsic to OPM. However, the derivation did not account for RPR, which increases the effective noise and thus decreases the effective signal-to-noise ratio. The factor of two to three increase in effective noise indicated by the eigenvalue analysis of PSR B2020+28 and PSR B1929+10 is enough to attribute the observed dispersion in fractional circular polarization to the reduced signal-to-noise ratio caused by RPR. Similarly, Kramer et al. (2002) found that the distribution of fractional circular polarization in the Vela pulsar was much wider than what was expected from the off-pulse instrumental noise. RPR could account for the excess noise in the emission

from Vela and, as mentioned above, may be the Gaussian emission component described by Cairns et al. (2003). McKinnon & Stinebring (2000) attributed excess polarization fluctuations in PSR B2020+28 to on-pulse instrumental noise, but their noise model could not account for all the observed fluctuations. The RPR revealed by the eigenvalue analysis can easily account for the excess fluctuations. RPR also causes the linear polarization to be slightly overestimated. When reporting the results of pulsar polarization observations, it is common practice to subtract a bias offset caused by the off-pulse instrumental noise from the computed values of linear polarization. While the bias value of

$$\langle L \rangle = \sigma_N \sqrt{\pi/2} \quad (35)$$

is relevant for data recorded off the pulse, the actual value may be much larger on the pulse where RPR can occur.

$$\langle L \rangle = \sqrt{(\sigma_P^2 + \sigma_N^2)\pi/2} \quad (36)$$

The OPM statistical model requires fluctuations in mode polarization amplitudes to observe the switching between modes. Similarly, moding will not be observed if the polarization amplitudes do not fluctuate. If the polarization amplitude fluctuates, one might reasonably expect the total intensity to fluctuate, also (MS1; MS2). Consequently, the model predicts that OPM should occur where the radiation is heavily modulated (§ 2.3). This is clearly the case for PSR B2020+28 and PSR B1929+10, as shown in Figures 2 and 6. The presence of OPM elongates the polarization ellipsoid, giving it a large axial ratio. For both pulsars, the axial ratio is large where the modulation index is also high. The axial ratio in PSR B1929+10 is relatively constant across much of its pulse, and its modulation index remains constant over a similar range in pulse longitude. In PSR B2020+28, both the axial ratio of the polarization ellipsoid and the intensity modulation index are large at the same locations within the pulse, primarily in the pulse peaks and wings. As mentioned in § 3.1, the intensity fluctuations are Gaussian and the modulation index is $\beta < 0.3$ near the center of the PSR B2020+28 pulse. The polarization data in this region are consistent with the occurrence of only one polarization mode. This observation raises the intriguing possibility that both polarization modes do not occur where intensity fluctuations are Gaussian. Stated another way, perhaps both polarization modes occur only where the modulation index exceeds some critical value, $\beta_c \simeq 0.3$.

The longitudinal extent of OPM determined from the eigenvalue analysis (Fig. 6) is different from what has been determined in previous analyses. MS2 calculated the mode-separated pulse profiles of PSR B0525+21 and PSR B2020+28. The model used in their analysis neglected RPR, and their results indicate that both modes occur at all locations within the pulse of each pulsar. However, the eigenvalue analysis presented in this paper reveals the presence of RPR and suggests that only one mode occurs near the center of the

PSR B2020+28 pulse. Using PA histograms, SCRWB found that OPM extended over a limited range of pulse longitudes. The elongated Q-U-V clusters may be a better indicator of OPM because, like the bin 90 data in PSR B1929+10, the PA histograms may only reveal the presence of one mode although both modes actually occur. Therefore, the longitudinal extent of OPM may be slightly greater than what is documented in SCRWB.

RPR complicates the mode separation technique presented in MS2. The technique assumes that two superposed modes, each completely polarized, are the only components of the emission. The simplicity of this assumption allows the mode intensities and polarizations to be calculated from the average values of the measured Stokes parameters. The occurrence of RPR introduces another variable in the model (e.g. Eqns. 32 - 34), and the mode separation is then indeterminate unless some simplifying assumption regarding RPR can be made. The dominant effect of RPR upon the results presented in Figures 4 and 5 of MS2 will be to reduce the intensities and polarizations of the modes at all pulse longitudes. This effect may be small because the magnitude of RPR estimated in this analysis appears to be small in relation to the total intensity of the emission (Fig. 6).

The results of single-pulse polarization observations are notoriously difficult to summarize and report, owing to the extreme variability of pulsar polarization and the large volume of data. The analysis developed here is a new method for presenting and interpreting the results of these types of observations. It is significantly different from previous data presentation methods. The results of some of the first single-pulse polarization observations were reported by plotting the raw Q-U-V data for a series of single pulses (e.g., Lyne, Smith, & Graham 1971). These seminal observations showed that pulsar polarization can be quite high and highly variable. Although the orientation of the polarization vector is somewhat difficult to visualize with this data presentation method, it readily illustrates the polarization associated with the total intensity of a limited number of pulses. MTH reported the results of their single-pulse polarization observations as multiple polarization ellipses plotted across the total intensity profiles of about a dozen, consecutive, individual pulses. The radiation's polarization state is immediately obvious with the MTH data presentation method. These observations were some of the first to reveal conclusively that OPM occur in the emission. SCRWB and Backer & Rankin (1980) presented the results of their single-pulse polarization observations as histograms of fractional circular polarization, fractional linear polarization, and PA. The histograms, which are particularly well-suited for documenting the occurrence of OPM, are statistical summaries that conveniently illustrate how the polarization fluctuates across the pulse. The polarization data recorded for a large number of pulses can be reported with this method. However, the histograms do not indicate the instantaneous orientation of the radiation's polarization vector because the circular and linear polarization data are reported separately. The data presentation method developed in this paper focuses

on a detailed investigation of a very large number of polarization samples at a single pulse longitude at the expense of both the total intensity information and a more global, instantaneous view of the polarization at other pulse longitudes. The method immediately shows the orientation of the radiation’s polarization vector, reveals the presence of OPM through the elongation of the data point cluster, and indicates the presence of RPR through the inflation of the cluster. Data presented in this manner can be readily interpreted in the context of other mechanisms that cause polarization fluctuations.

The objective of most radio polarization observations is to determine where the tip of a polarization vector resides in Poincaré space. This is done simply by averaging the individual Stokes parameters Q, U, and V. The tip of the vector is the centroid of the Q-U-V data point cluster, and it can be located more precisely by reducing the cluster size (i.e. the instrumental noise) through increased bandwidth and longer integration times. But as shown with the eigenvalue analysis and the statistical model of radio polarimetry (McKinnon 2003b), more polarization information is available to the radio astronomer. The unique ability to measure all Stokes parameters simultaneously at radio wavelengths also allows the astronomer to determine the cluster’s size, shape, and orientation. The physical processes that create polarization fluctuations can be investigated by measuring all geometrical properties of the cluster.

5. CONCLUSIONS

In summary, an eigenvalue analysis has been developed for the interpretation of pulsar polarization data. The analysis is based upon a three-dimensional statistical model of radio polarimetry and allows the linear and circular polarization of pulsar radio emission to be interpreted together, instead of separately as has been done typically in the past. The model is generally consistent with polarization observations of PSR B1929+10 and PSR B2020+28. The analysis clarifies the origin of polarization fluctuations in pulsar radio emission. The observed excess dispersion in PA is caused by the isotropic inflation of the Q-U-V data point cluster. The cluster inflation is not consistent with random fluctuations in PA and is attributed to RPR in the received pulsar signal. The presence of RPR may contribute to the depolarization of the emission at high radio frequency. A comparison of the model with the observational data suggests that OPM are superposed. OPM occur where the emission is heavily modulated, and may only occur where the modulation index exceeds a critical value, $\beta_c \simeq 0.3$. The analysis also reveals deviations from mode orthogonality in the circular polarization of PSR B1929+10.

I thank Dan Stinebring for providing the data used in the analysis. I thank Tim Hankins and an anonymous referee for constructive comments on the paper. I am grateful for the hospitality of the NRAO staff in Green Bank, WV, where this paper was written. The Arecibo Observatory is operated by Cornell University under cooperative agreement with the National Science Foundation.

REFERENCES

- Backer, D. C. & Rankin, J. M. 1980, *ApJS*, 42, 143
- Cairns, I. H., Johnston, S., & Das, P. 2003, *MNRAS*, 343, 512
- Cairns, I. H., Das, P., Robinson, P. A., & Johnston, S. 2003, *MNRAS*, 343, 523
- Cordes, J. M. 1976a, *ApJ*, 208, 944
- Cordes, J. M. 1976b, *ApJ*, 210, 780
- Fisher, N. I, Lewis, T., & Embleton, B. J. J. 1987, *Statistical Analysis of Spherical Data*, (Cambridge: Cambridge)
- Hankins, T. H., Kern, J. S., Weatherall, J. C., & Eilek, J. A., 2003, *Nature*, 422, 141
- Helfand, D. J., Manchester, R. N., & Taylor, J. H. 1975, *ApJ*, 198, 661
- Karastergiou, A., Kramer, M., Johnston, S., Lyne, A. G., Bhat, N. D. R., & Gupta, Y., 2002, *A&A*, 391, 247
- Karastergiou, A., Johnston, S., & Kramer, M., 2003, *A&A*, 404, 325
- Kramer, M., Johnston, S., & van Straten, W., 2002, *MNRAS*, 334, 523
- Lyne, A. G., Smith, F. G., & Graham, D. A. 1971, *MNRAS*, 153, 337
- Manchester, R. N., Taylor, J. H., & Huguenin, G. R. 1973, *ApJ*, 179, L7
- Manchester, R. N., Taylor, J. H., & Huguenin, G. R. 1975, *ApJ*, 196, 83 (MTH)
- McKinnon, M. M. 1997, *ApJ*, 475, 763
- McKinnon, M. M. 2002, *ApJ*, 568, 302
- McKinnon, M. M. 2003a, *ApJ*, 590, 1026
- McKinnon, M. M. 2003b, *ApJS*, 148, 519
- McKinnon, M. M. & Stinebring, D. R. 1998, *ApJ*, 502, 883 (MS1)
- McKinnon, M. M. & Stinebring, D. R. 2000, *ApJ*, 529, 435 (MS2)
- Morris, D., Graham, D. A. & Sieber, W. 1981, *A&A*, 100, 107

- Radhakrishnan, V. 1999, in ASP Conf. Ser. 180, Synthesis Imaging in Radio Astronomy II, ed. G. B. Taylor, C. L. Carilli, & R. A. Perley (San Francisco: ASP), 671
- Radhakrishnan, V. & Cooke, D. J. 1969, *Astrophys. Lett.*, 3, 225
- Rickett, B. J. 1975, *ApJ*, 197, 185
- Stinebring, D. R., Cordes, J. M., Rankin, J. M., Weisberg, J. M., & Boriakoff, V. 1984, *ApJS*, 55, 247 (SCRWB)
- Xilouris, K. M., Kramer, M., Jessner, A., & Wielebinski, R. 1994, *A&A*, 288, L17